Korean J. Chem. Eng., 36(12), 2008-2022 (2019)
DOI: 10.1007/s11814-019-0384-x

pISSN: 0256-1115
eISSN: 1975-7220

Evaluation of novel Mg/Al/Ni-BaFe ternary layered hydroxides uptake of methyl orange dye from water

Nuhu Dalhat Mu'azu*,†, Nabeel Jarrah, Mukarram Zubair*, Mohammad Saood Manzar*, Taye Saheed Kazeem***, and Mamdouh Al-Harthi****,*****

*Department of Environmental Engineering, Imam Abdulrahman Bin Faisal University, Dammam 31451, Saudi Arabia
**Department of Chemical Engineering, Mutah University, Karak 61710, Jordan
***Department of Civil Environmental Engineering, King Fahd University of Petroleum & Minerals, Dhahran 31261, Saudi Arabia
****Department of Chemical Engineering, King Fahd University of Petroleum & Minerals, Dhahran 31261, Saudi Arabia
*****Center of Research Excellences in Nanotechnology, King Fahd University of Petroleum & Minerals, Dhahran 31261, Saudi Arabia

(*Received 11 May 2019 • accepted 4 September 2019*)

Abstract−MgAlNi-BaFe ternary layered hydroxide (UMLDH) and its calcined (CMLDH) form were synthesized and tested as adsorbents for methyl orange dye (MO) uptake from water. The adsorptive performances of the new magnetic nanocomposites were modeled, evaluated and optimized via response surface methodology (RSM). The UMLDH and CMLDH maximum removal efficiency and adsorption capacities data were fitted into RSM models with insignificant lack of fit (p-values<0.05) and high R^2=0.991-0.997. The UMLDH and CMLDH MO adsorption capacities increased with decrease in both pH and initial MO concentration and decreased when the temperature was increased. Under optimal operating conditions, pseudo-second-order described kinetics of MO sorption on the nanocomposites, while the Freundlich isotherm gave the best fits for both the two adsorbents. The MO uptake simultaneously incorporated both mono and multi-layer surface adsorption involving strong electrostatic attraction and chemical interactions between MO and the adsorbents surface functional groups. Respectively, the obtained maximum Langmuir theoretical sorption capacity of 715.44 and 708 mg/g, indicated profoundly improved MO sorption capacities compared with many other magnetic-LDHs. These results demonstrate the potential of MgAlNi-BaFe as excellent adsorbents for effective remediation of dyes wastewater effluents.

Keywords: Barium Ferrite LDH, MgAlNi Nanocomposites, Methyl Orange Dye Uptake, Response Surface Methodology

INTRODUCTION

Compared with many other treatment technologies, adsorption technique has popularly received increased interest for decontamination of dye wastewater discharges from many industries. This has been attributed to its adeptness, cost-effectiveness and ease of operations. Layered double hydroxides have been categorized as a class of nanocomposites with superlative characteristics for efficient removal of dyes and other pollutants from water and wider range of environmental applications [1-3]. Consequently, considerable efforts have been made towards developing LDH with improved functionalities, particularly in the area of adsorption [4,5]. In the recent decade, the emergence of magnetized LDHs nanocomposites has led to the identification of these materials when used as adsorbents to exhibit higher capacities for uptake of dyes from water [5-8]. Layered double hydroxides (LDH), a popular name given to various groups of anionic clays or hydrotalcite clay, are identified as unique materials for the increased interest they attract for the wide range of roles they play in wastewater and water treatment [9], catalysis [1], biomedical treatment [2] and polymer industry [9,10]. This could be attributed to the achievable special morphology and greater flexibility in terms of chemical composition during synthesis, which in turn opens the doors for improving their anion exchange abilities. Consequently, this has led to the emergence of different classes of hybridized nanocomposite LDH employed for effective remediation of wastewater containing harmful substances with higher adsorptive performance than their precursors [11,12]. Moreover, additional unique property of the magnetized forms of LDH adsorbents is their ability to easily separate the spent residue materials from the water purified by simply applying a magnetic field [7,13]. The magnetic MZIF-67 composite reported by Yang et al. [14] showed the highest sorption capacity for methyl orange (738 mg/g). Similarly, other researchers reported using different types of magnetic nanocomposites with some amended features like Zr-MOFs composites [15], magnetic ferrite magnetic nanoparticles [16] and chitosan/Al_2O_3/magnetic iron oxide [17] and other non-magnetized adsorbents [18,19] yielded good removal of MO and other dyes from water. The performance of these magnetized materials has been reported [7,14,15,17,20-28] with MZIF-67 nanocomposites yielding adsorption capacity of up to 738 mg/g [14] However,

†To whom correspondence should be addressed.
E-mail: dalhat@gmail.com
Copyright by The Korean Institute of Chemical Engineers.

till date, research on synthesis and testing of magnetic LDH for removal of pollutants for removal of dyes from aqueous phase are still evolving compared to other classes of adsorbents [5,15,24,29,30]. Thus, this present work reports synthesis of new MgAlNi-BaFe ternary layered hydroxide (UMLDH) and its calcined (CMLDH) form using co-precipitation technique and their subsequent characterization and utilization for removal of MO from water. MO, an anionic dye that is discharged in wastewater effluent from numerous kinds of industries needs to be eliminated prior to discharge due to its potential detrimental consequences to the ecosystem [31]. Thus, under different experimental conditions, performance of the tested adsorbents for MO adsorption was modeled, evaluated and optimized using response surface methodology (RSM) and ANOVA. Moreover, the mechanisms and kinetics of MO removal by adsorbents were also investigated.

MATERIALS AND METHODS

1. Materials

Magnesium nitrate hexahydrate [$Mg(NO_3)_2{\cdot}6H_2O$, Sigma Aldrich Co., USA], Barium Ferrite [$BaFe_{12}O_{19}$ nanopowder, Aldrich, France], Aluminium nitrate nonahydrate (Sigma-Aldrich, Germany), Nickel (II) nitrate hexahydrate (Carlo Erba reagents, France), Sodium hydroxide and hydrochloric acid were purchased from PanReac AppliChem (Darmstadt, Germany) and Eurostar (Liverpool, UK), respectively. These chemicals and all other reagents used were of high purity (>97%) and were used as purchased. Millipore filtering machine-processed deionized water of high quality was used throughout the study.

2. Methyl Orange Absorbate

MO dye was used to test the adsorptive performance of the new UMLDH and CMLDH adsorbents. MO known as Sodium 4-[(4-dimethylamino)phenylazo]benzenesulfonate ($C_{14}H_{14}N_3NaO_3S$; density 1.28 g/cm^3 and molecular weight 327.33 g/mol) was purchased from Sigma Aldric, France. MO, an anionic dye has 13025 color index and 0.5 g/100 mL solubility in water at 20 °C with the structural forms under different pH conditions depicted in Fig. 1 [32]. While it is red at pH<3.2 (acid-stable form), it turns yellow at pH>4.4 (alkali stable form), a color change attributed to transition from azo structure (chromophore) to quinoid structure [32].

3. Synthesis and Characterization of UMLDH and CMLDH

Co-precipitation technique was employed for the synthesis of the UMLDH nanocomposites as follows. First, about 500 mg of BaFe was ultrasonicated for 30 minutes in 0.2 M NaOH solution at 100 amplitude. The solution was then mixed with salt (precursor) solution at a target mass of Mg, Ni and Al of 5.12 g, 2.91 g, 3.75 g, i.e., ratio of 2 : 1 : 1. Afterwards, the precursor salt was prepared using 50 ml deionized water controlling at pH 10 while under vigorous stirring with 2-3 drops of hydrazine used as reducing agent. Then, the pH was further maintained using 1.0 M NaOH solution. The obtained suspension was then refluxed for 24 h at 90 °C while continuously maintaining stirring using magnetic set-up prior to undergoing centrifuging. Any impurity on the obtained UMLDH was removed by washing with using pure ethanol and deionized and then dried under 90 °C for 24 hours. The UMLDH was used as the precursor for the CMLDH synthesis under N_2 environment supplied at 130 mL min^{-1} and temperature of 400 °C for 4 h. More details on this procedure are described elsewhere [33,34]. The synthesized UMLDH and CMLDH were then characterized for their X-Ray diffraction (XRD) patterns and crystallography using Rigaku MinifeFlex II diffractometer with parameters step-size, scan rate and 2θ range set at 0.03°, 3°/min and 5-70°, respectively. Meanwhile, the Fourier transform-infrared (FTIR) spectra) were obtained using Nicolet 6700 spectrometer (operated at room temperature), while thermal decomposition patterns of the synthesized nanocomposites were undertaken by heating at 10 °C /min using thermogravimetry analyzer (TGA) using SDT-600 TGA/DSC. Scanning electron microscopy (SEM) and EDS data were obtained using TIMA TESCAN SEM Integrated system to obtain the microstructure and elemental composition of the samples. The zeta potentials of the UMLDH and CMLDH nanocomposites dispersed in 10 mM NaCl solution were determined from their electrophoretic mobility based on Smoluchowski model using a Malvern Zetasizer Nano-ZS (Malvern, USA).

4. RSM Modeling Experimental Design

Due to its many merits and effectiveness as a technique for evaluation and assessment of adsorption and other environmental processes using fewer number of experimental trials, RSM was adopted in this study. This was to enable development of response models while incorporating curvature, correlating operational parameters and their interactive effects on the investigated responses using analysis of variance (ANOVA) as well as optimizing the MO adsorption on the new adsorbents [35,36]. As such, 3^3 faced centered central composite design (FC-CCD) was used under the RSM technique to investigate temperature (25-45 °C), initial MO concentration (20-100 mg/L), and initial pH (2-6) (designated as A, B and C, respectively) on removal efficiency (R) and adsorption capacity (q_e) for the UMLDH and CMLDH MO uptake. The levels and ranges of these operational conditions were selected as per our earlier works [5,34]. For a number of independent variables of k, FC-CCD consisted of 3^k, $2k$, and k designated for factorial, axial and replicated central experimental runs, thereby giving a total of nineteen (19) required adsorption tests as given in Table 1. The central runs were duplicated to investigate the experiment replicability and to assess level of experimental error while the tests were carried out in randomized order to avoid influences of unforeseen factors for ensuring data credibility and quality [36,37]. Design Expert version 9 [38] was employed for fitting the data obtained from the experimental

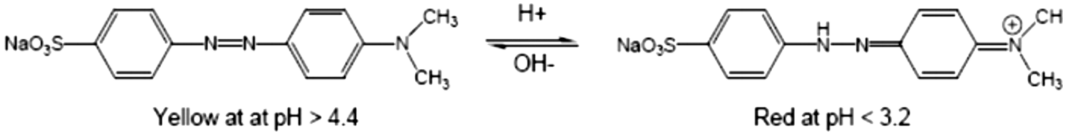


Fig. 1. Different structural forms of methyl orange under acidic and basic stable conditions in aqueous phase [1].

Table 1. RSM Experimental design and results for sorption of MO onto UM-LDH and CM-LDH

Test#	Operating conditions			Removal efficiency (%)		Adsorption capacity (mg/g)	
	Temp (°C)	Initial MO conc (mg/L)	Initial pH	UMLDH	CMLDH	UMLDH	CMLDH
	A	B	C	Y1	Y2	Y3	Y4
R1	25	20	2	54.3	52.9	65.2	63.4
R2	45	20	2	58.2	54.3	69.8	65.2
R3	25	100	2	40.0	38.1	240.2	228.5
R4	45	100	2	42.0	40.8	251.8	244.9
R5	25	20	6	39.9	35.5	47.8	42.6
R6	45	20	6	44.2	39.5	53.0	47.4
R7	25	100	6	29.2	28.0	175.3	167.8
R8	45	100	6	27.6	26.1	165.5	156.8
R9	25	60	4	49.9	47.9	179.6	172.4
R10	45	60	4	51.9	50.6	187.0	182.0
R11	35	20	4	63.3	60.0	76.0	71.9
R12	35	100	4	49.2	48.2	295.3	289.1
R13	35	60	2	35.5	33.7	127.6	121.1
R14	35	60	6	31.8	30.0	114.3	107.8
R15	35	60	4	51.1	48.9	183.8	176.0
R16	35	60	4	52.8	51.6	190.0	185.8
R17	35	60	4	49.3	47.8	177.3	172.0
R18	35	60	4	54.3	52.9	65.2	63.4
R19	35	60	4	58.2	54.3	69.8	65.2

program into the generalized RSM model in Eq. (1) for developing the response models:

$$y = \beta_0 + \sum_{i=1}^{k} \beta_i x_i + \sum_{i=1}^{k} \beta_i x_i^2 + \sum_{i=1}^{k-1} \sum_{j=2}^{k} \beta_{ij} x_i x_j + \varepsilon \quad (1)$$

where y=RSM model's dependent variable, i.e., predicted response; β_0, β_i, β_{ij}, β_{ii}=RSM model's coefficients; x_i, x_j=experimental independent variables.

5. MO Batch Adsorption Tests

Based on serial dilution, MO concentrations ranging 20-100 mg/L were made from 1,000 mg/L MO stock solution, all prepared using deionized water. Using a Lab Companion SK-600 Benchtop shaker run at 120 rpm, MO uptake experiments were conducted in a 50 ml glass-flask containing 30 ml of MO solution at required concentration, initial pH and temperature (as per experimental design in Table 1) and agitation time of 180 minutes. pH alteration was achieved using 0.1 M NaOH or 0.1 M HNO_3 solution and a pH meter (HANA pH meter). After each test, sample was immediately filtered through 0.45 micron filter and then centrifuged at 3,500 rpm for 5 minutes for total separation of the spent UMLDH and CMLDH from the resulting effluent. The supernatant MO residual concentration was then measured immediately, using a Jasco V-670 UV-Visible spectrometer set at absorbance wavelength 340-580 nm. The q_e and R were obtained from Eqs. (2) and (3) as follows:

$$q_e = \frac{C_o - C_e}{W} * V \quad (2)$$

$$R = \frac{C_o - C_e}{C_o} * 100 \quad (3)$$

W=Mass of the adsorbent, g; q_e=adsorption capacity, mg/g; R=MO Removal efficiency; V_L=Solution volume, liters; C_o=MO concentration before adsorption, mg/L and C_f=MO concentration after adsorption, mg/L.

RESULTS AND DISCUSSION

1. Adsorbents Characterization Analysis

The UMLDH and CMLDH SEM images are presented in Fig. 2. Both adsorbents images show rough and homogeneously compacted surfaces of nanoparticles [39]. For the composite CMLDH (Fig. 2(b)), the structure and morphology differs slightly from that of the UMLDH (Fig. 2(a)), indicating a softer nanostructure with likely more uniform pores. Table S1 provides the BET surface area and pore size distributions data, which shows that additional calcination induced on the precursor adsorbent (UMLDH) led to significant reduction in the BET surface area from 132.378 m^2/g to 81.919 m^2/g (for the CMLDH). Also, the corresponding average pore volume and radius changed from 0.32 cm^3/g, 54.77 Angstrom (5.477 nm) and 0.226 cm^3/g, 81.92 Angstrom (8.192 nm), respectively. Thus, the pore distribution data of UMLDH and CMLDH (supplementary data Fig. S1 and Table S1) implies that both UMLDH and CMLDH are characterized with surfaces that are mesoporous [40].

These characteristics of the two nanocomposites indicate that they can serve as good adsorbents [40]. The available functional groups on the UMLDH and CMLDH that greatly influence MO uptake revealed by the FTIR analyses are given in Fig. 3. While, the bands of the (C-O and Al-O) and O-H groups are typically associ-

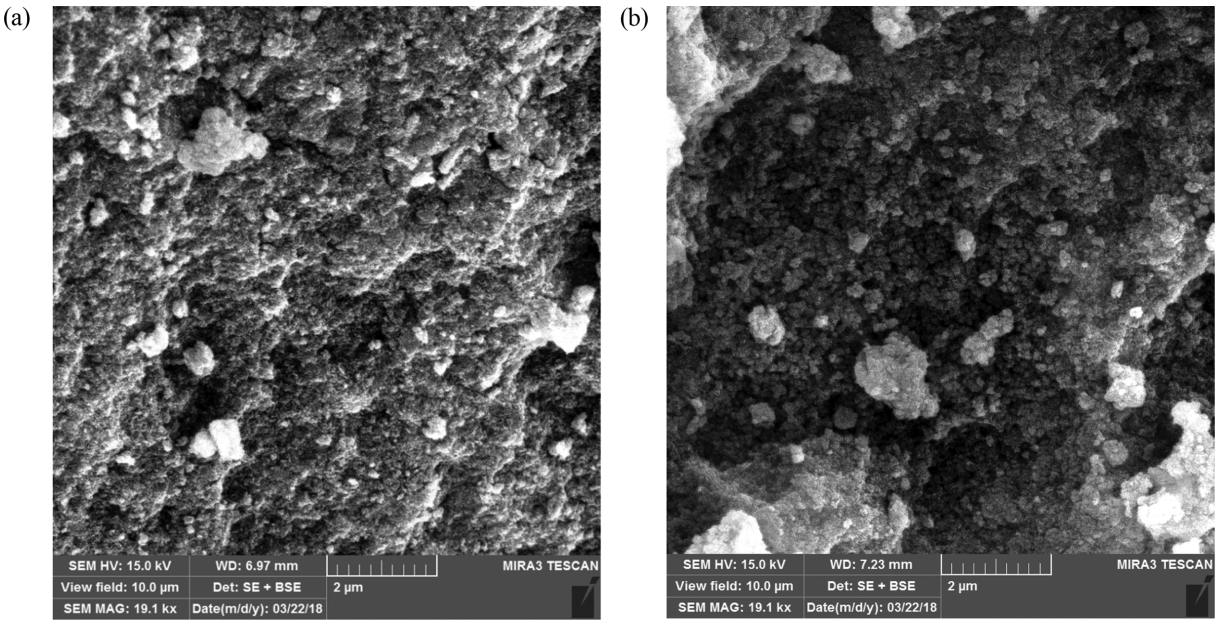


Fig. 2. SEM images of (a) UMLDH and (b) CMLDH nanocomposites.

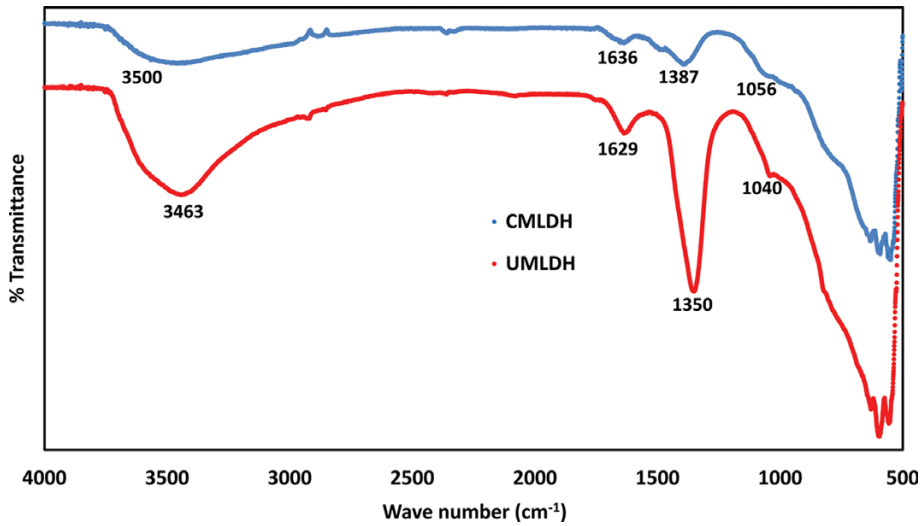


Fig. 3. FTIR patterns for UMLDH (below) and CMLDH (above) nanocomposites.

ated with 1,000 cm^{-1} and 3,000-3,600 cm^{-1} peaks, respectively. The peaks shown at 1,040 cm^{-1} and 1,350 cm^{-1} and stretching vibration are identified for C-O-C bond and NO_3^- ion, respectively [41,42]. Calcination was expected to help in production of oxygen containing functional groups, which could profoundly increase adsorptive performance [43]. Considering that the UMLDH peaks observed at 1,335 cm^{-1} and 3,463 cm^{-1} underwent slight shift and significant reduction in the FTIR of the CMLDH (Fig. 3), suggesting that the expected improvement on the important functional groups did not occur. This is corroborated by the EDS analysis results in Fig. S2 which show a weight percent decrease in the amount of elemental oxygen from 41.58 to 38.15 after calcination. This reduction might have resulted in the loss of some oxygen-carrying functional groups as well as changes in the pore characteristics (Table S1) that invariably affected the adsorptive performance of the CMLDH. The EDS Fig. S2 also confirms the presence of Mg, Al, Ni, Fe and Ba along with carbon and oxygen in the two nanocomposites.

Fig. 4 presents the XRD of BaFe and the MgAlNi-LDHs (i.e., UMLDH and CMLDH). The well-defined crystalline MgAlNi-LDHs possesses the characteristic peaks of LDH with a basal spacing of 0.775 nm. The peaks at 2θ=11.4° and 22.4° are assigned to the (003) and (006) planes, respectively. There also exist other peaks at 2θ=34.5°, 38.9°, 45.9° and 61.1° indexed to the (009), (015), (018) and (113) planes, respectively [44]. It could be observed that the introduction of the BaFe nanoparticles into the MgAlNi-LDH slightly led to reduction in crystallinity of UMLDH, which is evident in the reduction of peak intensity of the (003) diffractogram.

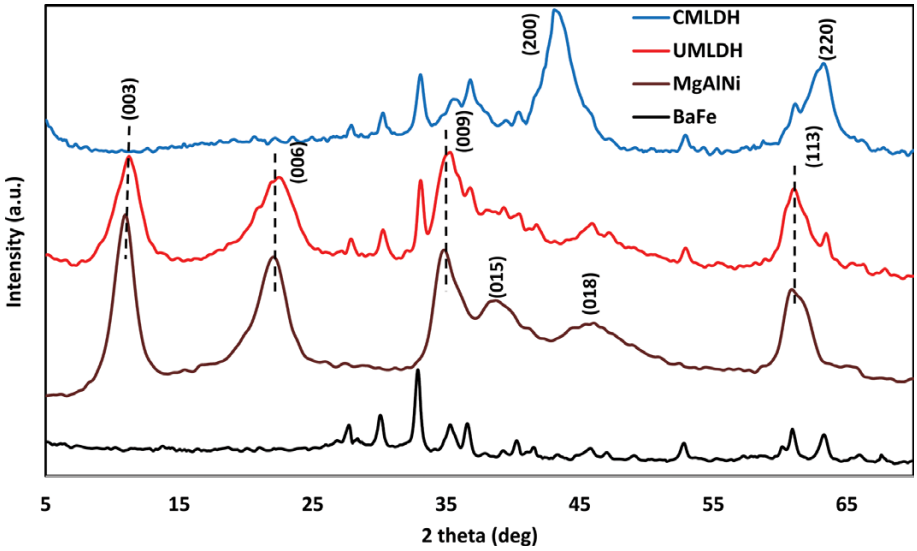


Fig. 4. XRD analyses for BaFe, MgAlNi LDH, UMLDH, and CMLDH.

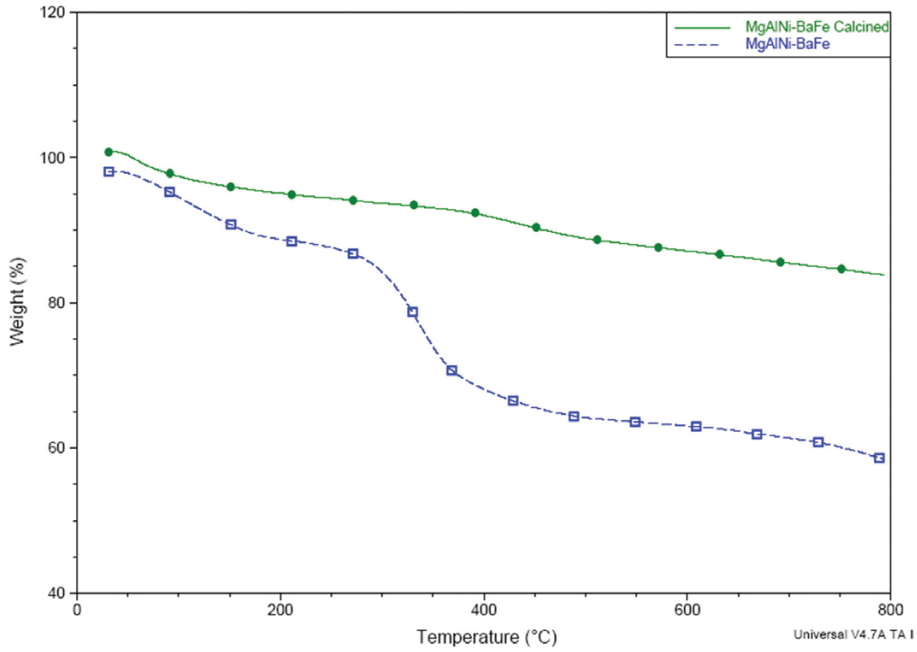


Fig. 5. TGA analysis for UMLDH (above) and CMLDH (below) nanocomposites.

It is also observed that some original peaks of BaFe become conspicuous in UMLDH, indicating successful synthesis of magnetized MgAlNi-BaFe-LDH [45-47]. Upon calcination of the UMLDH, the peaks initially present vanished while new peaks corresponding to (200) and (220) planes associated with mixed metal oxide formation become apparent. This development indicates the destruction of pristine lamellar structure of the UMLDH and the production of CMLDH. The mean crystallite sizes of UMLDH and CMLDH computed based on the XRD analysis according to Scherrer equation [48,49] are 7.96 and 12.06 nm, respectively.

Under nitrogen environment ramped at up to 800 °C (at 10 °C/min), Fig. 5 presents the TGA analysis illustrating UMLDH and CMLDH weight loss, which suggests different response of the two adsorbents under thermal changes. While the UMLDH exhibited about 40% loss in weight, the CMLDH underwent about half of such a value in weight loss. This was attributed to the removal of water when UMLDH was transformed into CMLDH, which rendered the CMLDH having higher stability when subjected to thermal variations. Accordingly, the CMLDH was susceptible to undergoing two modes of mass reduction related decarbonation (DC) and the removal anions within the interlayer, which was expected to have resulted in mixed metal oxides (MMO) production [50]. On the other hand, raising the temperature could have resulted in up to three separate modes weight losses which include (i) for tem-

Table 2. ANOVA of UMLDH and CMLDH for MO sorption models

	Y_1		Y_2		Y_3		Y_4	
	F-value	p-Value	F-value	p-Value	F-value	p-Value	F-value	p-Value
Model	99.01	<0.0001	58.20	<0.0001	206.63	<0.0001	90.23	<0.0001
A	5.94	0.0449	2.38	0.1613	0.94	0.3760	0.40	0.5435
B	275.58	<0.0001	108.69	<0.0001	631.36	<0.0001	204.60	<0.0001
C	3.66	0.0973	2.01	0.1945	2.33	0.1876	34.98	0.0004
AB	4.18	0.0801			0.22	0.6622	0.00	0.9710
AC	0.67	0.4395	0.15	0.7105	1.44	0.2841		
BC			0.85	0.3845	44.86	0.0011	13.20	0.0067
A2	1.87	0.2140	27.25	0.0008	1.10	0.3433	0.89	0.3735
B2	60.41	0.0001	210.55	<0.0001	2.81	0.1548		
C2	374.42	<0.0001			239.49	<0.0001	85.01	<0.0001
A^2B					51.62	0.0008	18.16	0.0028
A^2C	20.22	0.0028	13.02	0.0069	11.44	0.0196		
AB^2								
BC^2								
LOF	0.438775	0.8021	0.84	0.6340	0.903297	0.5636	2.72	0.2932

[a]Significance established at 5% (p-value<0.05)
[b]Significance established at 10% (p-value<0.1); LOF=Lack of fit

peratures <220 °C which led to up to 15% weight reduction due to physisorbed as well as intercalated and H_2O got eliminated [51], (ii) for 220-410 °C temperature range, which resulted in 20% loss due to removal of nitrates via dihydroxylation (DH), other interlayer anions and DC [52], (iii) >410 °C temperature for the last stage loss, which is comparatively smaller, though it was expected to have led to generation of MMO due to more dehydroxylation and decarbonation [50].

The zeta potentials of UMLDH and CMLDH as a function of pH are shown in Fig. S3. It is observed that the surfaces of the adsorbents are positively charged for the whole pH range of 2 to 12. The nanocomposites surfaces obtained their highest positivity at pH 2 (≥+37 mV), which significantly dropped at pH 12 (<+4 mV) and this will significantly affect the adsorption capacity. Reported pK_a of MO at 3.76 [53] indicated that at pH<3.76, the MO molecules exist as cations, while for pH>pK_a, the MO molecules exist as anions. This indicates that the highest adsorption for MO on a positively charged surface should occur at pH>3.76. Due to electrostatic attraction, the highest removal of MO is expected to occur at pH 4 between the negatively charged MO molecules and highly positive UMLDH and CMLDH.

2. Development of RSM Models for UMLDH and CMLDH MO Adsorption

The experimental data (R and q_e) obtained for the batch adsorption tests are provided in Table 1. For the UMLDH and CMLDH , the maximum R ranged between 27.6-63.3% and 26.1-60.0%, while the maximum q_e ranged between 47.8 to 295.3 mg/g and 42.6 to 289.1 mg/g, respectively. This clearly suggests that changes in the operating conditions significantly influence the performance of the tested adsorbents. Moreover, the high q_e values obtained indicate good performance of the two magnetized composite adsorbents tested despite the moderate removal efficiency obtained. Thus, using multiple nonlinear regressions, the different data sets in Table 1 were fitted into Eq. (1) to obtain the best fitted RSM models given in Eqs. (4) to (7), where Y_1 and Y_2 represent UMLDH and CMLDH MO removal efficiency models and Y_3 and Y_4, UMLDH and CMLDH MO adsorption capacity models, respectively. These models best describe the experimental data according to high significant model's terms with no aliaseness and *p*-value<0.0001 (Table 2), respectively [54]. Using ANOVA, only terms (single effect, quadratic and/or cubic terms) that significantly impacted on the respective model's (response) performance are used (Table 2) [36]. For instance, Y_1 ANOVA indicated that significant terms for UMLDH MO removal efficiency include all factors A, B (at *p*-values<0.05) and C (at *p*-values<0.1) that possessed direct influence (i.e., main effects), only 2-way interaction AB (at *p*-values<0.1), C^2 and B^2 squared effects and the cubic effect A^2C (all *p*-values<0.05) are higher significant model terms. However, the A^2 terms though independently, insignificant (*p*-value>0.1 and 0.05), but exerted significant influence under interaction with another factor in the A^2B (*p*-value<0.05), thereby significantly contributing towards the models prediction's accuracy. Similar interpretation can be deduced for the other remaining three developed models in Eqs. (4)-(6) and ANOVA in Table 2, respectively.

$$Y_1\,(\%)=50.31+1.054\,A-7.179B-1.85C-0.9887AB-0.396AC+1.142A^2+6.494B^2-16.166C^2-4.861A^2C \quad (4)$$

$$Y_2\,(\%)=48.71+0.902A-6.091B-1.85C-0.251AC+1.0385A^2+5.892B^2-16.3782C^2-5.271A^2C \quad (5)$$

$$Y_3\,(mg/g)=181.199+1.896A+109.68B-6.66C-1.0125AB-2.618AC-14.618BC+3.9465A^2+6.3165B^2-58.36352C^2-35.0625A^2B-16.508A^2C \quad (6)$$

$$Y_4\,(mg/g)=176.787+2.154A+108.6B-20.082C-0.1425AB-13.7925BC+5.8149A^2-56.885C^2-36.173A^2B \quad (7)$$

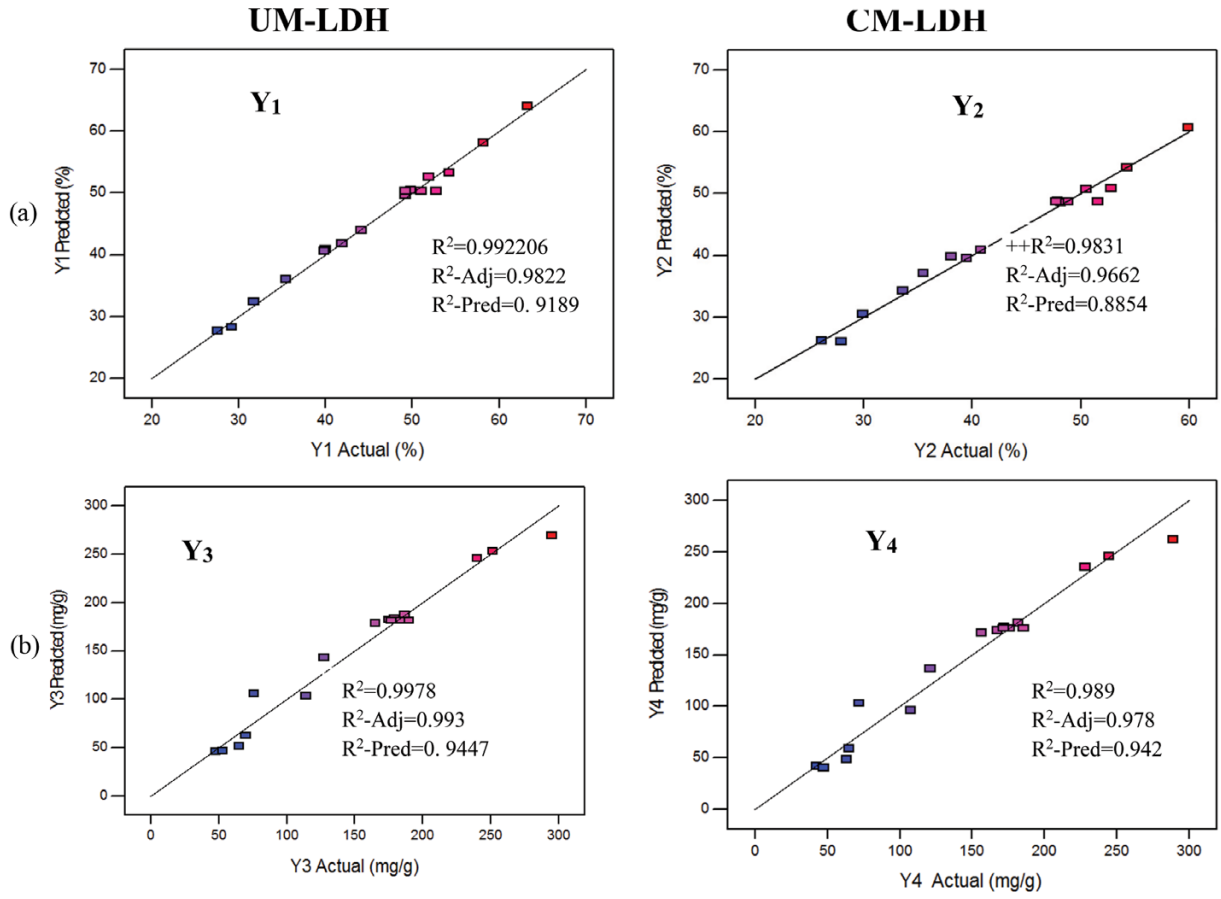


Fig. 6. Experimental versus predicted values for UMLDH and CMLDH MO (a) removal efficiency and (b) adsorption capacity models.

3. Pareto Charts Assessments of RSM Models Terms

Pareto charts presented in Fig. S4 visually depict the comparative evaluation of level of contributions of individual operating conditions and their 2-way interaction. The Pareto bars' height proportionally reveals the relative contributions of the terms in the developed models on the responses investigated (Y_1 to Y_4 in Fig. S4); the higher the bar, the more the contribution. On the other hand, the blue and orange charts indicate synergistic and antagonistic effects respectively [37]. Accordingly, for R models (i.e., Y_1 and Y_2 in Fig. S4), factors C and B were the major parameters whose influence outweighed that of factor A and the interacting terms. Similarly, for the q_e response models Y_3 and Y_4, factors C and B were also the most significant factors, though their interacting effects BC play also a major role towards controlling MO uptake by both UMLDH and CMLDH. For both the adsorbents, the Pareto analysis indicates that factor A (i.e., temperature effect) is more manifested in the removal efficiency models (A, AB and AC), while exerting lesser influence on the adsorption capacity for MO uptake. Generally, the Pareto charts analysis, dependently shows the least significant influence of factor A compared to factor B on efficacy of MO removal for the magnetized adsorbents, which is in conformity with the ANOVA.

4. RSM Models Validation

The quality of the RSM models describing MO adsorption onto the UMLDH and CMLDH developed was evaluated based on coefficients of determination (R^2) of 0.992, 0.983, 0.999 and 0.989 for Y_1, Y_2, Y_3 and Y_4, respectively. These values are, respectively, in conformity with the high values of the non-R^2 (predicted and adjusted) obtained as given in Fig. 6, satisfying the requirements for RSM models [36]. This is further demonstrating the high prediction abilities of the models to predict the obtained MO adsorption test data as also presented in Fig. 6 [55-57]. Meanwhile, the linear normal probability plots for the models given in Fig. S5 indicate satisfying normality assumption of the RSM models with all the *p*-values being statistically significant (i.e., $p<0.05$ or $p<0.1$) as given in Table 2). These models' diagnostics suggest the suitability of employing the developed UMLDH and CMLDH MO sorption models for assessing and evaluating the influence of independent variables on the investigated responses [35,36].

5. Effect of Parameters on R and q_e

The dependencies of the investigated responses on experimental operating conditions are illustrated in 3D plots obtained based on the developed RSM models (Figs. 7 and 8) which are discussed below.

5-1. Effect of Operating Conditions on R for UMLDH and CMLDH

For both the UMLDH and CMLDH adsorbents, Fig. 7 shows the influence of the operating conditions on efficacy of MO removal. The MO removal was significantly affected when the initial pH was increased from 2 to 6, which was initially decreased reaching the peak value at around pH 3-4 for both UMLDH and CMLDH

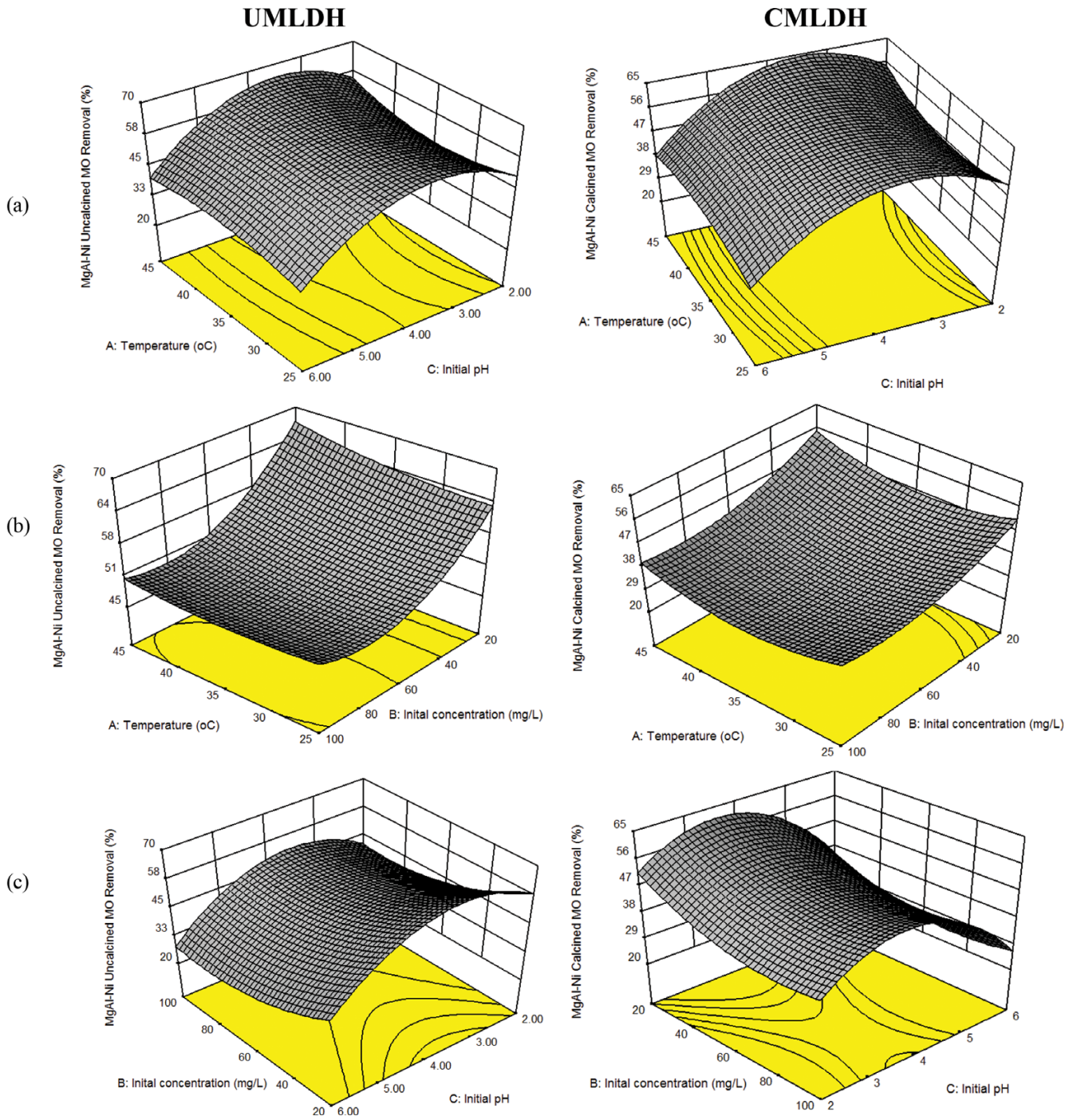


Fig. 7. Effect of operational conditions on MO removal efficiency for UMLDH and CMLDH.

(Fig. 6(a) and 6(c)). The maximum R of 63.3 and 60% obtained occurred when operations were at A=25 °C, B=20 mg/L and C=4. However, the R values continued to decrease as C was increased from 2-6 reaching lowest values of 39.9% and 35.5% at C=6, respectively. However, factor A had the less significant interactive effects on C (p-values of AC all >0.1 as observed earlier), though it had significantly contributed to R at higher level interaction which led to the observed visually displayed curvature effect in Fig. 7(a) and C (p-values of A^2 and A^2C all <0.1 as observed earlier). The effect of C on the tested magnetized LDHs obtained is in line with other studies, which revealed that even within the acidic range, higher pH values are susceptible to dwindle dyes aqueous uptake [41,42, 58]. Though, there is the issue of instability and possible solubilization known with LDH, yet the majority of the reported works on LDH established that maximum adsorptive capacities for LDHs are obtained within pH range of 2 to 4. The decline of adsorptive performance of most LDH at higher pH (even within acid range) was mainly attributed to introduction of more OH^- ions when pH

was increased which reduced the possibility of accommodating more of the anionic dyes within the active site of surface functional groups [59]. Thus, at solution pH 2-4, the existence of abundant H^+ ions in solution facilitates higher tendencies towards promoting protonation of the UMLDH and CMLDH surface functional groups. As such, stronger electrostatic attractive forces are enhanced between the MO anion molecules and the positively charged oxygen functionalities of UMLDH and CMLDH, which eventually improved the R [51,60]. However, for both UMLDH and CMLDH point of zero charge (PZC) of 8.32 and 9.46, respectively, were far above the range investigated (PZC>6). This suggests that both adsorbents' surfaces were mostly protonated during all the tests [60], indicating lesser influence of PZC within the investigated pH range. The dependencies of adsorptive performances of UMLDH and CMLDH on factor B in relation to other variables are presented in Fig. 6(b) and 6(c). Regardless of the A and C values, the R significantly increased when the factor B was decreased. The greater effect of C and B was further demonstrated by the

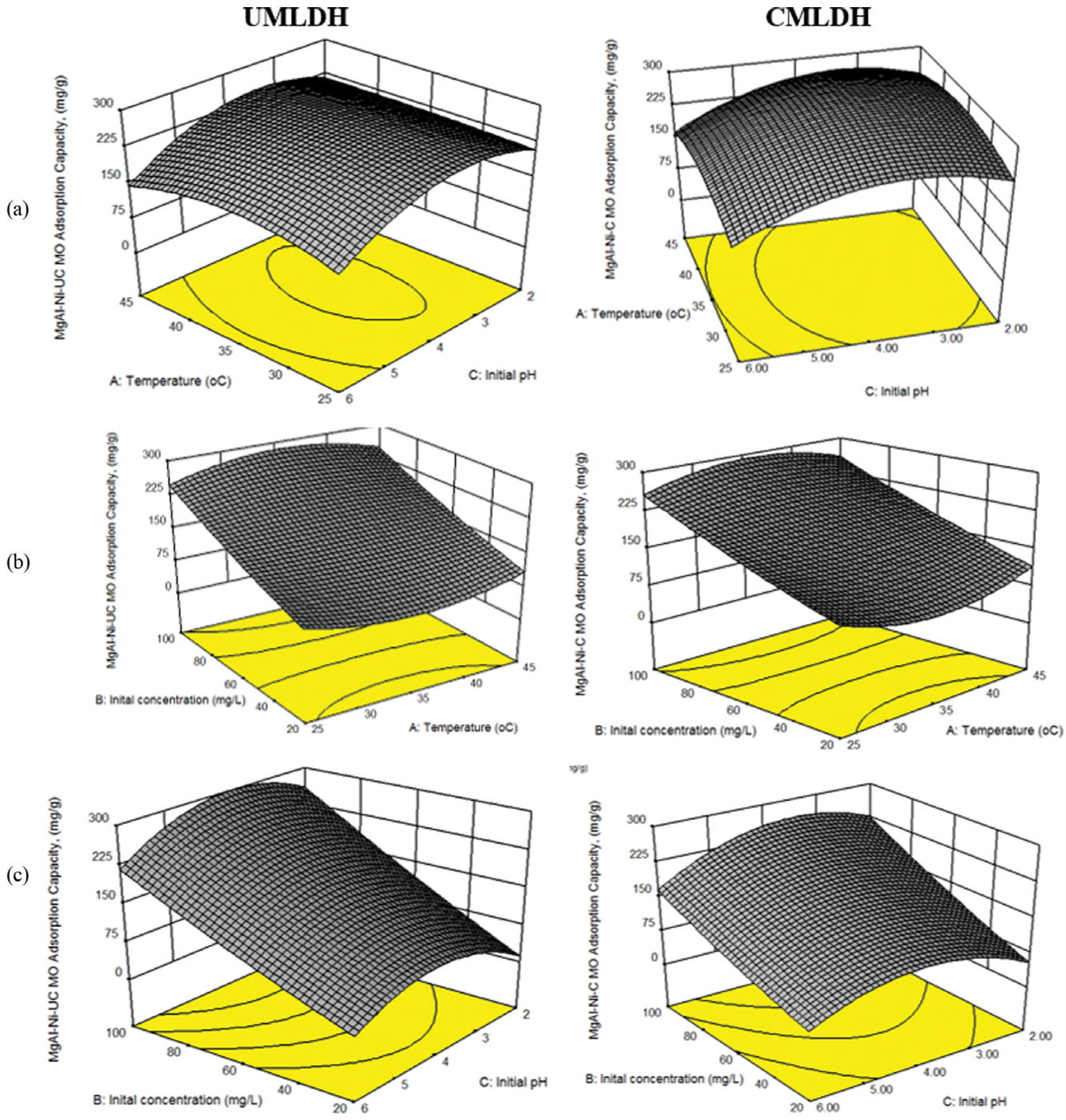


Fig. 8. Effect of operational conditions on MO adsorption capacity for UMLDH and CMLDH.

greater interactive influence they exerted on the R as observed earlier. For both UMLDH and CMLDH, with increase in factor A, there was a tendency toward improving the MO removal (Fig. 7(a) and 7(b)) despite the lowest influence impacted by the temperature. This was attributed to the greater influences of the other factors which dwarfed the temperature effects (Pareto charts in Fig. S4 and least *p*-values in Table 2). Nevertheless, this results imply that much higher temperature was likely to have positively impacted on the adsorptive performances of the tested adsorbents.

5-2. Effect of Operating Conditions on q_e for UMLDH and CMLDH

The 3D and their corresponding contour plots presented in Fig. 8 visually illustrate the influence of the investigated experimental parameters on UMLDH and CMLDH adsorption capacities for removal of MO from aqueous phase. As in the case of R, the adsorption capacity for both adsorbents initially increased as the pH increased from 2 reaching a maximum value at around pH 4. Afterwards, increasing the pH value led to a decline in the q_e (Fig. 8(a) and 8(c)). In contrast to the observed trend of R, increasing MO initial concentration significantly improved the q_e for both adsorbents, impacting higher influence than the pH (Fig. 8(b) and 8(c)), which is clearly manifested in the Pareto chart (Fig. S4). Consequently, the maximum q_e of 295.3 and 289.1 mg/g was attained when the C and B were at 4 and 100 mg/L, which drastically reduced to 47.8 and 42.6 mg/g when they were changed to 6 and 20 mg/L, respectively. Collectively, Fig. 8(a) and 8(b), ANOVA as well as Pareto charts in Fig. S4 suggest that changing the temperature conspicuously impacted on the adsorptive performances of UMLDH and CMLDH, though at much lower degree of influence compared with the other two factors. Based on the models and statistical evaluations, the temperature effect is more manifested on R than on q_e. The improvement in q_e with increase in MO initial concentration was attributed to induced increase in higher interactions between the available adsorbents' active sites as more of the MO molecules were added to the solution [61]. Similar to the removal efficiency, calcination of the parent UMLDH did not improve the MO sorption capacity, instead it reduced it slightly. This small reduction in the performance of the UMLDH compared to that of the CMLDH was speculated to be due to the physico-chemical changes (structure, pore size distribution and reduction in some active sites after the calcination [62] as suggested by the oxygen carrying functional groups reduction at 3,457 and 1,355 cm^{-1} of the FTIR despite the improved BET surface area (i.e., from 109.6 to 154.1 m^2/g) after the calcination (Fig. 3). This corroborates earlier findings by other authors who reported better sorption of MO dye on precursor LDH over a ternary LDH of larger BET surface area [63]. The presence of higher Cu^{2+} was responsible for the higher sorption capacity of the precursor due to induction of low basicity and higher electrostatic affinity of the MO onto the cationic LDH [63].

5-3. Analysis of FTIR and XRD before and after Adsorption

After the MO adsorption tests, the spent UMLDH and CMLDH FTIR analyses in Fig. S6 were generated in order to compare them with the fresh ones, which indicated that the peaks at the interlayer of C=O and NO_3^- at 1,750-1,642 cm^{-1} and 1,292 and 1,358 cm^{-1} symmetric stretching had shifted. Moreover, the intensity for Si-O-Si and Si-O stretching vibrations at 1,001 and 1,217 cm^{-1} peaks, respectively, underwent reduction and disappearance. Similarly, the XRD pattern of CMLDH analyzed after MO adsorption (Fig. S7) indicates the existence of MO molecules following its uptake, considering that there was somewhat increase in shift of 003 basal spacing to 0.728 nm (2θ=12.140) from 0.778 nm (2θ= 11.360) in the interlamellar space of the CMLDH. This shift has been associated with MO-LDH anions exchange occurring during the MO adsorption process [64].

6. RSM Optimization

As a result of variability in performance of an adsorbents due to changes in several experimental parameters, numerical optimization has been identified as a tool employable to help in identifying the optimal operation conditions. This is because of the difficulties involved in getting optimality by mere inspection of data when all variables (dependent and independent) are taken into consideration. Thus, the unique desirability function capability of Design-Expert® software was employed for optimizing MO adsorption onto UMLDH and CMLDH under four (4) scenarios target goals provided in Table S2 and S3. The desirability value which ranged between 0 to 1, designated as worst to best scenario, was obtained using numerical algorithms that identify best operational conditions as per the targeted set goals (for all variables). In this study, the main target objectives were to maximize R and q_e based on the RSM response models Y_1 and Y_2; Y_3 and Y_4, respectively, while minimizing operating temperature for the different initial concentrations. All the UMLDH and CMLDH results obtained from the optimization scenarios 1-4, as provided in Table S2 and S3 constantly indicated that the best solutions with high desirability were obtained at when the C=4 and both A and B values are kept at highest levels. Also, reducing A to its lowest (25 °C) did not significantly affect the dye adsorption when factor A was ≥60 mg/L. Thus, at higher initial concentration, temperature has less impact on the target responses. However, at lower initial concentration, higher temperature is expected to yield better adsorption performance. Consequently, additional experiments on the effect of dosage as well as equilibrium and kinetics studies were conducted for MO adsorption onto the UMLDH and CMLDH at the optimal conditions of, A= 25 °C, B=100 mg/L and C=4.

7. Effect of Dosage on q_e

To experimentally explore the achievable q_e, the effect of adsorbent dosage was investigated within the range of 2-20 mg at the obtained optimal RSM conditions. The results plotted in Fig. 9 show that at 2 mg dosage, the maximum obtained q_e of 709.4 and 693.4 mg/g gradually decreased reaching the minimum values of as low as 144.8 and 137.28 mg/g for the highest investigated dosage of 20 mg. Conversely, the corresponding achievable R for MO was significantly increased from about 10% to 70% for both the two adsorbents. When initial concentration was fixed and the adsorbents dosage increased, better R for MO was expected due to the increase in the abundant sites (more UMLDH and CMLDH adsorptive functional groups) that are actively partaking in the MO adsorption. However, depending on the initial concentration, increasing the amount of the UMLDH and CMLDH may result in increase in redundant active sites on the adsorbents that cannot be utilized in accommodating the MO molecules. Corroborating the earlier observations, UMLDH consistently demonstrated a slightly improved performance over the CMLDH for all the different dosages.

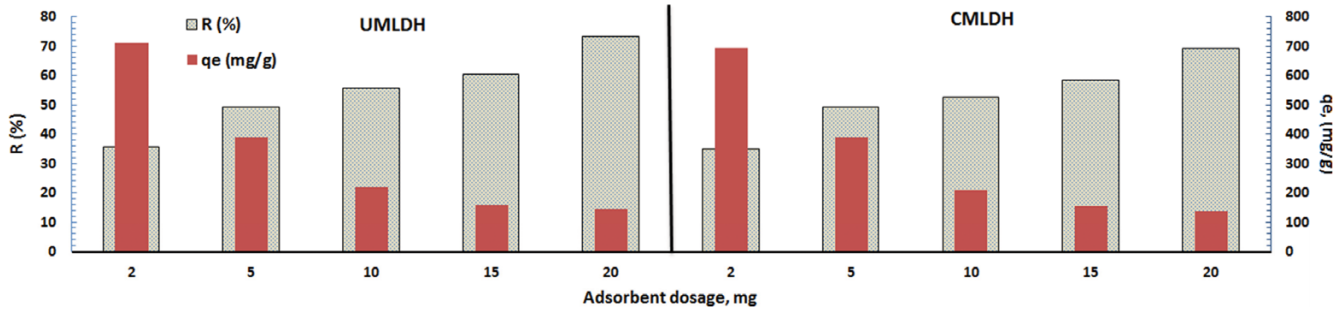


Fig. 9. Effect of dosage on adsorption capacity and removal efficiency for UMLDH and CMLDH.

8. Equilibrium and Kinetic Studies

8-1. Adsorption Isotherm Study

To elaborate the interaction of MO molecules on the surfaces of UMLDH and CMLDH composites, Dubinin-Radushkevich (DR), [65] Freundlich [66], Langmuir [67] and Temkin [68] models were employed on equilibrium data obtained under the optimal conditions (pH 4, dosage 5 mg, temperature 298 K, contact time 180 minutes) obtained from RSM. The non-linear form of the four models and their respective estimated parameters yields are given in Table 4, while Fig. 9 demonstrates the plots of the experimental equilibrium data against the models predictions 298 K. For both composites, the Freundlich isotherm gave the best fits (R^2 of 0.895 and 0.876 for UMLDH and CMLDH, respectively) with sequence of fit in the order: Freundlich>Langmuir>Tempkin>DR adsorption isotherm model. Thus, for UMLDH and CMLDH, the adsorption of MO has satisfactorily fitted well with Freundlich isotherm, though the Langmuir comparatively performed to a lesser extent. This indicates that the surface of composites exhibited homogeneous and heterogeneous morphology. The maximum adsorption capacity calculated using the Langmuir isotherm was found to be 715.44 and 708 mg/g for UMLDH and CMLDH, respectively. Collectively, the kinetics and isotherm results showed that the MO uptake could be recognized as simultaneously incorporating both mono and multi-layer surface adsorption involving strong electrostatic attraction and chemical interactions among MO molecules and surface functional groups of the new tested magnetized nanocomposites. The Freundlich isotherm constant (1/n) indicates the fraction of heterogeneity and intensity of adsorption are 0.80 and 0.89 for UMLDH and CMLDH, respectively. The values below unity further direct higher heterogeneity and favorably the sorp-

Table 3. Parameters of nonlinear pseudo first, pseudo second order kinetic models under the optimal conditions (pH 4, dosage 5 mg, temperature 298 K, contact time 180 minutes)

		Pseudo first order $q_t = q_e(1+e^{-k_1 t})$			Pseudo second order $\frac{t}{q_t} = \frac{t}{k_2 q_e^2} + \frac{t}{q_e}$		
	$q_{e\,(exp)}$	q_e	k_1	R^2	q_e	$k_2 \times 10^{-5}$	R^2
UMLDH	434.4	1378.8	0.11	0.865	769.23	0.9	0.979
CMLDH	436.24	1469.38	0.10	0.806	714.28	1.5	0.981
		Elovich $q_t = \frac{1}{\beta}\ln(\alpha\beta) + \frac{1}{\beta}\ln(t)$			Intra particle diffusion $q_t = k_d t^{1/2} + C$		
		α	β	R^2	C	K_d	R^2
UMLDH	434.4	18.33	0.008	0.947	−46.36	34.01	0.973
CMLDH	436.24	17.89	0.008	0.945	−48.96	33.87	0.980

Table 4. Parameters of non-linear Langmuir, Freundlich, Tempkin and DR isotherm models under the optimal conditions (pH 4, dosage 5 mg, temperature 298 K, contact time 180 minutes)

	Langmuir $q_e = \frac{q_{max} K_L C_e}{1 + K_L C_e}$			Freundlich $q_e = K_F C_e^{1/n}$			Tempkin $q_e = B\ln(AC_e)$			DR $q_e = q_s\left(\exp\left(-K\left(RT\ln\left(1+\frac{1}{C_e}\right)\right)^2\right)\right)$		
	$q_{max,\,(mg/g)}$	K_L	R^2	K_F	1/n	R^2	B	A	R^2	q_s	$K \times 10^{-5}$	R^2
UMLDH	715.44	0.016	0.844	15.32	0.80	0.895	108.59	0.27	0.756	236.82	1.15	0.55
CMLDH	708.15	0.014	0.810	10.39	0.89	0.876	111.82	0.23	0.714	229.29	1.48	0.51

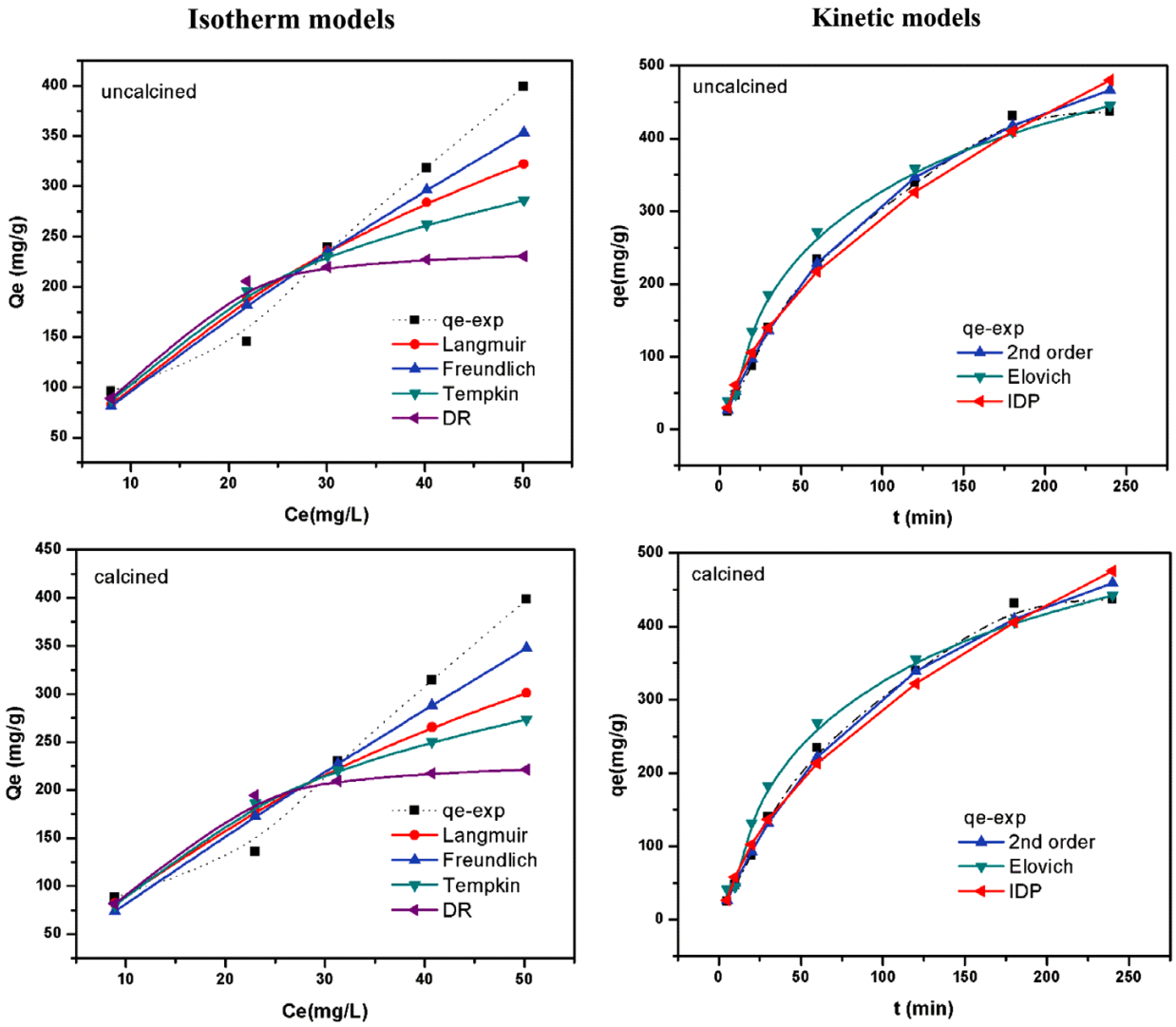


Fig. 10. Plots for experimental data vs non-linear isotherm and kinetic models' predictions for (a) UMLDH and (b) CMLDH.

tion system of both magnetic LDHs and MO molecules. The high uptake of MO molecules is attributed to the combined effect of NiMgAl and barium ferrite resulting in excellent surface characteristics exhibiting high surface area and abundant surface functionalities (C-O, Si-O, Si-O-Si, NO_3, Al-O, C-O-C).

8-2. Kinetic Study

The kinetics of MO dye adsorption onto UMLDH and CMLDH was evaluated by employing non-linear forms of four kinetic models (pseudo-first order, pseudo-2nd order, Elovich and intraparticle diffusion models [69]) under the RSM optimal conditions (pH 4, MO concentration 100 mg/L, temperature 298 K, dosage 5 mg). The adsorption kinetic experimental data versus the fitted models are displayed in Fig. 10. The models' estimated parameters given in Table 3 show that the correlation coefficient R^2 of pseudo-second-order model for the two adsorbents (0.979 and 0.981, respectively) is significantly higher than that of other kinetic models. This is further manifested in the close agreement of the predicted q_e for the pseudo-second-order model (769.28 and 714.28 mg/g, respectively) with the values obtained for experimental as well as equilibrium studies. This implies that pseudo-second-order model fitted well with experimental data for the MO-UMLDH and MO-CMLDH sorption process. Therefore, based on the assumption upon which the pseudo-second order kinetic model was developed, it is suggested that the mechanism was mainly dominated via chemical interaction between MO molecules and adsorbent surface functional groups [42]. Additionally, the actual rate determining phases were explored using intraparticle diffusion model, which indicated a very good fitting (0.973 and 0.98, respectively). Accordingly, this suggests that MO adsorption followed three major steps: (i) Fast adsorption rate within 30-50 minutes associated with surface adsorption on exterior active sites of adsorbents; this includes electrostatic attraction, chemical and ion-exchange interactions with surface functionalities (C=O and NO_3^-, Si-O and Si-O-Si) as confirmed by FTIR and XRD analysis after MO adsorption; (ii) Internal pore diffusion of MO molecules into the layers magnetic LDHs at slow rate, and (iii) Equilibrium step, which relates to saturation of binding sites [39]. Similar behavior was also reported in previous related studies [51,72].

Table 5. Reported magnetized LDH MO capacity compared with UMLDH and CMLDH

#	LDH name	Uptake capacity (mg/g)	Optimal pH	Time (hr)	Reference
1	UMLDH	763.35	4	3	This study
2	CMLDH	756.42	4	3	This study
3	Zr-MFCs	219	3	1	[15]
4	MZIF-67 composites	738	8.0	7	[14]
5	Ferrite magnetic nanoparticles	-	7	6	[29]
6	MIL-101(Cr)/RGO/$ZnFe_2O_4$	-	7.	00.833	[70]
7	Fe_3O_4/activated carbon nanocomposites	324.00	-	06.67	[20]
8	Fe_3O_4/MIL-101($Al_{0.9}Fe_{0.1}$)/NH_2	355.80	06.0	02.	[71]
9	Fe_3O_4@GO hybrid composite	039.95	2.	06	[22]
10	Magnetic maghemite (y-Fe_2O_3)/	029.4	2.91	9	[24]
11	Magnetized Graphene oxide/LDH	210.80	-	-	[25]
12	Chitosan/Al_2O_3/magnetic iron oxide	417	4	24	[17]

9. Comparison of UMLDH and CMLDH Performace with other Magnetic LDH

A summary of the comparison of the maximum obtained adsorption capacities of the UMLDH and CMLDH for MO, and other similar magnetic LDH nanocomposites that were reported recently in literature, is presented in Table 5 [14-17,20-22,24,25,72]. As can be seen from the table, the two LDH adsorbents reported in this present study performed excellently due to their higher and improved uptake capacity for MO (715.44 and 708 mg/g respectively) over most of the other hybrid magnetic LDH. Some of the listed LDH in Table 5 that exhibited comparative performance, though, needed longer equilibrium time compared to that of the new UMLDH and CMLDH. Hussaina et al. [46] reported 375 mg/g maximum adsorption capacity of calcined MgAlNi-LDH for MO uptake. Thus, the obtained capacities for UMLDH and CMLDH in this study indicate the great potential for improving the adsorptive capacity of the MgAlNi via incorporating the BaFe. This implies that the tested magnetic LDH presented here has great potential for deployment as adsorbents for remediation of wastewater contaminated with MO and other similar dyes.

CONCLUSION

MgAlNi-BaFe layered hydroxide hybrid nanocomposite was synthesized using co-precipitation technique and tested as an adsorbent for removal of methyl orange dye (MO) from water. The adsorptive performance of both the precursor uncalcined (UMLDH) and the calcined (CMLDH) composites was modeled, evaluated and optimized using response surface methodology (RSM) based on FC-CCD experimental design. The effects of initial MO concentration, initial pH and temperature on maximum removal efficiency and adsorption capacities were fitted into RSM models with insignificant lack of fit and high R^2=0.991-0.997, which is in conformity with the non-biased regression coefficients R^2-adjusted and R^2-predicted obtained. The adsorption capacity increased with decrease in pH and increase in initial MO concentration and tended to decrease with increase in temperature. Respectively, the maximum MO adsorption capacity of 715.44 and 708 mg/g was obtained at temperature 25 °C, pH 4 and 100 mg/L initial MO concentration, indicating a profound improvement of capacity of both adsorbents for MO aqueous adsorption compared with many other magnetized adsorbents. Pseudo-second-order described the kinetics of MO sorption on the nanocomposites, while the Freundlich isotherm gave the best fits with sequence of fit in the order Freundlich>Langmuir>Tempkin>DR adsorption model. The excellent performance of the new UMLDH and CMLDH compared with many other hybrid magnetic adsorbents suggests that they have great potentials for effective remediation of dyes contaminated water and wastewater.

ACKNOWLEDGEMENTS

Funding provided by King Abdul-Aziz City for Science and Technology (KACST) under NSTIP through Project No. 12-Env2229-46 at Imam Abdulrahman Bin Faisal University and the Center of Research Excellences in Nanotechnology King Fahd University of Petroleum & Minerals for synthesis and characterization of the adsorbents is acknowledged and appreciated.

SUPPORTING INFORMATION

Additional information as noted in the text. This information is available via the Internet at http://www.springer.com/chemistry/journal/11814.

REFERENCES

1. Z. P. Xu, J. Zhang, M. O. Adebajo, H. Zhang and C. Zhou, *Appl. Clay Sci.*, **53**, 139 (2011).
2. Y. Kuthati, R. K. Kankala and C.-H. Lee, *Appl. Clay Sci.*, **112-113**, 100 (2015).
3. M. Daud, M. S. Kamal, F. Shehzad and M. A. Al-Harthi, *Carbon*, **104**, 241 (2016).
4. N. N. Das, J. Konar, M. K. Mohanta and S. C. Srivastava, *J. Colloid Interface Sci.*, **270**, 1 (2004).
5. M. Zubair, M. Daud, G. McKay, F. Shehzad and M. A. Al-Harthi, *Appl. Clay Sci.*, **143**, 279 (2017).
6. L. Lu, J. Li, D. H. L. Ng, P. Yang, P. Song and M. Zuo, *J. Ind. Eng.*

Chem., **46**, 315 (2017).
7. R.-r. Shan, L.-g. Yan, K. Yang, S.-j. Yu, Y.-f. Hao, H.-q. Yu and B. Du, *Chem. Eng. J.*, **252**, 38 (2014).
8. Y. Wang, T. Du, L. Zhou, Y. Song, S. Che and X. Fang, *Korean J. Chem. Eng.*, **35**, 709 (2018).
9. M. Daud, M. S. Kamal, F. Shehzad and M. A. Al-Harthi, *Carbon*, **104**, 241 (2016).
10. R. Ma, Z. Liu, L. Li, N. Iyi and T. Sasaki, *J. Mater. Chem.*, **16**, 3809 (2006).
11. W. Peng, H. Li, Y. Liu and S. Song, *J. Mol. Liq.*, **230**, 496 (2017).
12. G. Huang, L. Jiang, D. Wang, J. Chen, Z. Li and S. Ma, *J. Mol. Liq.*, **220**, 346 (2016).
13. Y.-X. Wang, K. Gupta, J.-R. Li, B. Yuan, J.-C. E. Yang and M.-L. Fu, *Colloids Surf., A: Physicochem. Eng. Aspects*, **538**, 378 (2018).
14. Q. Yang, S. Ren, Q. Zhao, R. Lu, C. Hang, Z. Chen and H. Zheng, *Chem. Eng. J.*, **333**, 49 (2018).
15. L. Huang, M. He, B. Chen and B. Hu, *Chemosphere*, **199**, 435 (2018).
16. R.-G. Ciocarlan, E. M. Seftel, M. Mertens, A. Pui, M. Mazaj, N. N. Tusar and P. Cool, *Mater. Sci. Eng.: B*, **230**, 1 (2018).
17. B. Tanhaei, A. Ayati, M. Lahtinen and M. Sillanpää, *Chem. Eng. J.*, **259**, 1 (2015).
18. M. R. Abukhadra, M. Rabia, M. Shaban and F. Verpoort, *Adv. Powder Technol.*, **29**, 2501 (2018).
19. M. R. Abukhadra, A. Adlii and B. M. Bakry, *Int. J. Biol. Macromol.*, **126**, 402 (2019).
20. R.-S. Juang, Y.-C. Yei, C.-S. Liao, K.-S. Lin, H.-C. Lu, S.-F. Wang and A.-C. Sun, *J. Taiwan Inst. Chem. Engineers*, **90**, 51 (2018).
21. S. Bao, K. Li, P. Ning, J. Peng, X. Jin and L. Tang, *J. Taiwan Inst. Chem. Engineers*, **87**, 64 (2018).
22. V. Ganesan, C. Louis and S. P. Damodaran, *J. Environ. Chem. Eng.*, **6**, 2176 (2018).
23. Z. Zhang and J. Kong, *J. Hazard. Mater.*, **193**, 325 (2011).
24. R. Jiang, Y.-Q. Fu, H.-Y. Zhu, J. Yao and L. Xiao, *J. Appl. Polym. Sci.*, **125**, E540 (2012).
25. Z. Yang, S. Ji, W. Gao, C. Zhang, L. Ren, W. W. Tjiu, Z. Zhang, J. Pan and T. Liu, *J. Colloid Interface Sci.*, **408**, 25 (2013).
26. L. Adlnasab, M. Ezoddin, M. A. Karimi and N. Hatamikia, *Res. Chem. Intermediates*, **44**, 3249 (2018).
27. X. Wu, B. Li and X. Wen, *J. Nanopart. Res.*, **19**, 131 (2017).
28. Z. Jia, S. Li, J. Liu, Q. Qin and R. Zhu, *Bull. Mater. Sci.*, **38**, 1757 (2015).
29. R.-G. Ciocarlan, E. M. Seftel, M. Mertens, A. Pui, M. Mazaj, N. Novak Tusar and P. Cool, *Mater. Sci. Eng.: B*, **230**, 1 (2018).
30. H. Sun, L. Cao and L. Lu, *Nano Res.*, **4**, 550 (2011).
31. K. Cui, B. Yan, Y. Xie, H. Qian, X. Wang, Q. Huang, Y. He, S. Jin and H. Zeng, *J. Hazard. Mater.*, **350**, 66 (2018).
32. S. N. Basahel, T. T. Ali, M. Mokhtar and K. Narasimharao, *Nanoscale Res. Lett.*, **10**, 73 (2015).
33. N. D. Mu'azu, N. Jarrah, T. S. Kazeem, M. Zubair and M. Al-Harthi, *Appl. Clay Sci.*, **161**, 23 (2018).
34. M. Zubair, N. Jarrah, M. S. Manzar, M. Al-Harthi, M. Daud, N. D. Mu'azu and S. A. Haladu, *J. Mol. Liq.*, **230**, 344 (2017).
35. N. D. Mu'azu, M. H. Al-Malack and N. Jarrah, *Desalination Water Treat*, **52**, 7293 (2014).
36. M. H. Essa, N. D. Mu'azu, S. Lukman and A. Bukhari, *Soil and Sediment Contamination: An International J.*, **24**, 30 (2015).
37. N. D. Mu'azu, S. A. Haladu, N. Jarrah, M. Zubair, M. H. Essa and S. A. Ali, *J. Hazard. Mater.*, **342**, 58 (2018).
38. R. H. Myers and D. C. Montgomery, *Response Surface Methodology: Process and Product Optimization Using Designed Experiments*, Wiley, New York (1995).
39. Y. Vlamidis, E. Scavetta, M. Giorgetti, N. Sangiorgi and D. Tonelli, *Appl. Clay Sci.*, **143**, 151 (2017).
40. M. Hussein, A. Jaafar, A. Yahaya, M. Masarudin and Z. Zainal, *Int. J. Mol. Sci.*, **15**, 20254 (2014).
41. A. A. Oladipo and M. Gazi, *J. Water Process Eng.*, **2**, 43 (2014).
42. F. B. D. Saiah, B.-L. Su and N. Bettahar, *J. Hazard. Mater.*, **165**, 206 (2009).
43. S. Yang, L. Wang, X. Zhang, W. Yang and G. Song, *Chem. Eng. J.*, **275**, 315 (2015).
44. T. S. Kazeem, M. Zubair, M. Daud, N. D. Mu'azu and M. A. Al-Harthi, *Korean J. Chem. Eng.*, **36**, 1057 (2019).
45. S. Tang and H. K. Lee, *Anal. Chem.*, **85**, 7426 (2013).
46. H. Zaghouane-Boudiaf, M. Boutahala and L. Arab, *Chem. Eng. J.*, **187**, 142 (2012).
47. Z. Wang and X. Li, *High Perform. Polym.*, 0954008317716976 (2017).
48. P. Scherrer, *Nachr. Ges. Wiss. Göttingen*, **2**, 96 (1918).
49. R. Elmoubarki, F. Z. Mahjoubi, A. Elhalil, H. Tounsadi, M. Abdennouri, M. h. Sadiq, S. Qourzal, A. Zouhri and N. Barka, *J. Mater. Res. Technol.*, **6**, 271 (2017).
50. D. Chebli, A. Bouguettoucha, A. Reffas, C. Tiar, M. Boutahala, H. Gulyas and A. Amrane, *Desalination Water Treatment*, **57**, 22061 (2016).
51. M. Zubair, N. Jarrah, A. Khalid, M. S. Manzar, T. S. Kazeem and M. A. Al-Harthi, *J. Mol. Liq.*, **249**, 254 (2018).
52. M. N. Pahalagedara, M. Samaraweera, S. Dharmarathna, C.-H. Kuo, L. R. Pahalagedara, J. A. Gascón and S. L. Suib, *J. Phys. Chem. C*, **118**, 17801 (2014).
53. W. Yao, S. Yu, J. Wang, Y. Zou, S. Lu, Y. Ai, N. S. Alharbi, A. Alsaedi, T. Hayat and X. Wang, *Chem. Eng. J.*, **307**, 476 (2017).
54. N. D. Mu'azu, A. Usman, N. Jarrah and O. Alagha, *Soil and Sediment Contamination: An International J.*, **25**, 757 (2016).
55. G. Wang, S. Zhang, T. Li, X. Xu, Q. Zhong, Y. Chen, O. Deng and Y. Li, *RSC Adv.*, **5**, 58010 (2015).
56. G. Wang, S. Zhang, X. Xu, Q. Zhong, C. Zhang, Y. Jia, T. Li, O. Deng and Y. Li, *Sci. Total Environ.*, **569-570**, 557 (2016).
57. M. Shaban, M. R. Abukhadra, A. S. Mohamed, M. G. Shahien and S. S. Ibrahim, *J. Inorg. Organomet. Polym. Mater.*, **28**, 279 (2018).
58. Y. Lu, B. Jiang, L. Fang, F. Ling, J. Gao, F. Wu and X. Zhang, *Chemosphere*, **152**, 415 (2016).
59. L. Lu, J. Li, D. H. Ng, P. Yang, P. Song and M. Zuo, *J. Ind. Eng. Chem.*, **46**, 315 (2017).
60. N. Belhouchat, H. Zaghouane-Boudiaf and C. Viseras, *Appl. Clay Sci.*, **135**, 9 (2017).
61. A. Khalid and M. Zubair, *Arabian J. for Sci. Eng.*, **43**, 2167 (2018).
62. S. Karaca, A. Gürses, M. Ejder and M. Açıkyıldız, *J. Hazard. Mater.*, **128**, 273 (2006).
63. D. Bharali and R. C. Deka, *Colloids Surf., A: Physicochem. Eng. Aspects*, **525**, 64 (2017).
64. S. L. Wang, R. J. Hseu, R. R. Chang, P. N. Chiang, J. H. Chen and Y. M. Tzou, *Colloids Surf., A: Physicochem. Eng. Aspects*, **277**, 8

(2006).
65. C. Nguyen and D. D. Do, *Carbon*, **39**, 1327 (2001).
66. P. Monash and G. Pugazhenthi, *Environ. Prog. Sustainable Energy*, **33**, 154 (2014).
67. Y. X. Zhang, X. D. Hao, M. Kuang, H. Zhao and Z. Q. Wen, *Appl. Surf. Sci.*, **283**, 505 (2013).
68. K. Y. Foo and B. H. Hameed, *Chem. Eng. J.*, **156**, 2 (2010).
69. W. J. Weber and J. C. Morris, *J. Sanitary Eng. Division*, **89**, 31 (1963).
70. L. Nirumand, S. Farhadi, A. Zabardasti and A. Khataee, *Ultrason. Sonochem.*, **42**, 647 (2018).
71. S. Bao, K. Li, P. Ning, J. Peng, X. Jin and L. Tang, *J. Taiwan Inst. Chem. Engineers*, **87**, 64 (2018).
72. Y. Lu, B. Jiang, L. Fang, F. Ling, J. Gao, F. Wu and X. Zhang, *Chemosphere*, **152**, 415 (2016).

Supporting Information

Evaluation of novel Mg/Al/Ni-BaFe ternary layered hydroxides uptake of methyl orange dye from water

Nuhu Dalhat Mu'azu[*,†], Nabeel Jarrah[**], Mukarram Zubair[*], Mohammad Saood Manzar[*], Taye Saheed Kazeem[***], and Mamdouh Al-Harthi[**,*****]**

*Department of Environmental Engineering, Imam Abdulrahman Bin Faisal University, Dammam 31451, Saudi Arabia
**Department of Chemical Engineering, Mutah University, Karak 61710, Jordan
***Department of Civil Environmental Engineering, King Fahd University of Petroleum & Minerals, Dhahran 31261, Saudi Arabia
****Department of Chemical Engineering, King Fahd University of Petroleum & Minerals, Dhahran 31261, Saudi Arabia
*****Center of Research Excellences in Nanotechnology, King Fahd University of Petroleum & Minerals, Dhahran 31261, Saudi Arabia
(*Received 11 May 2019 • accepted 4 September 2019*)

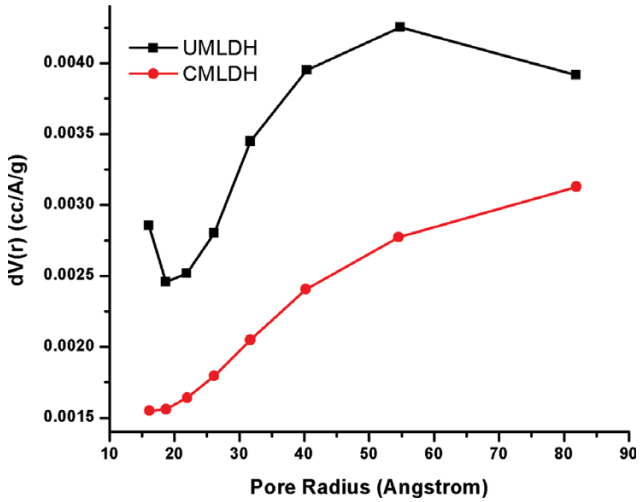


Fig. S1. (a) Pore size distribution for UMCLD and CMLDH.

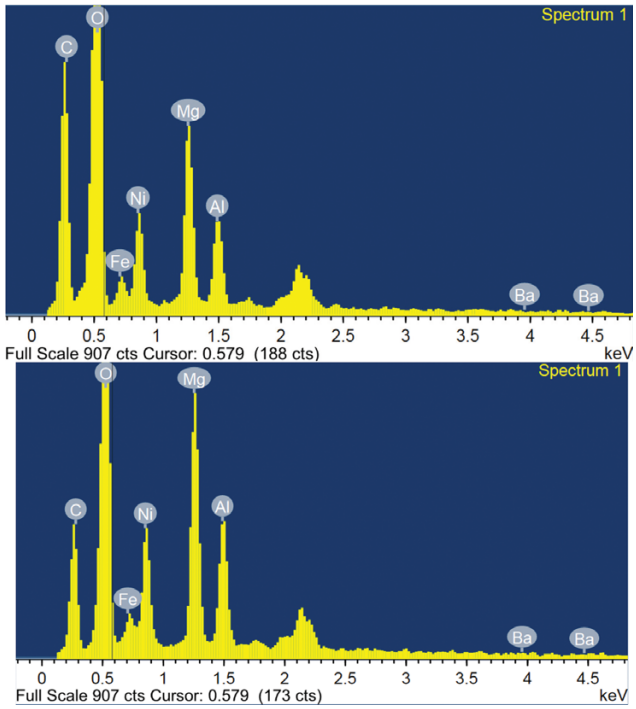


Fig. S2. EDS Analysis of UMLDH (above) and CMLDH (below).

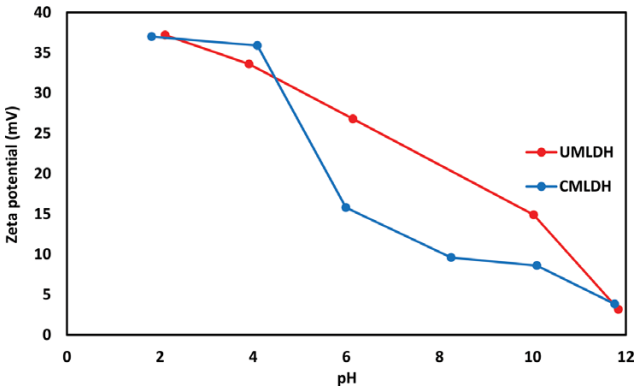


Fig. S3. Zeta potential plot for UMLDH and CMLDH.

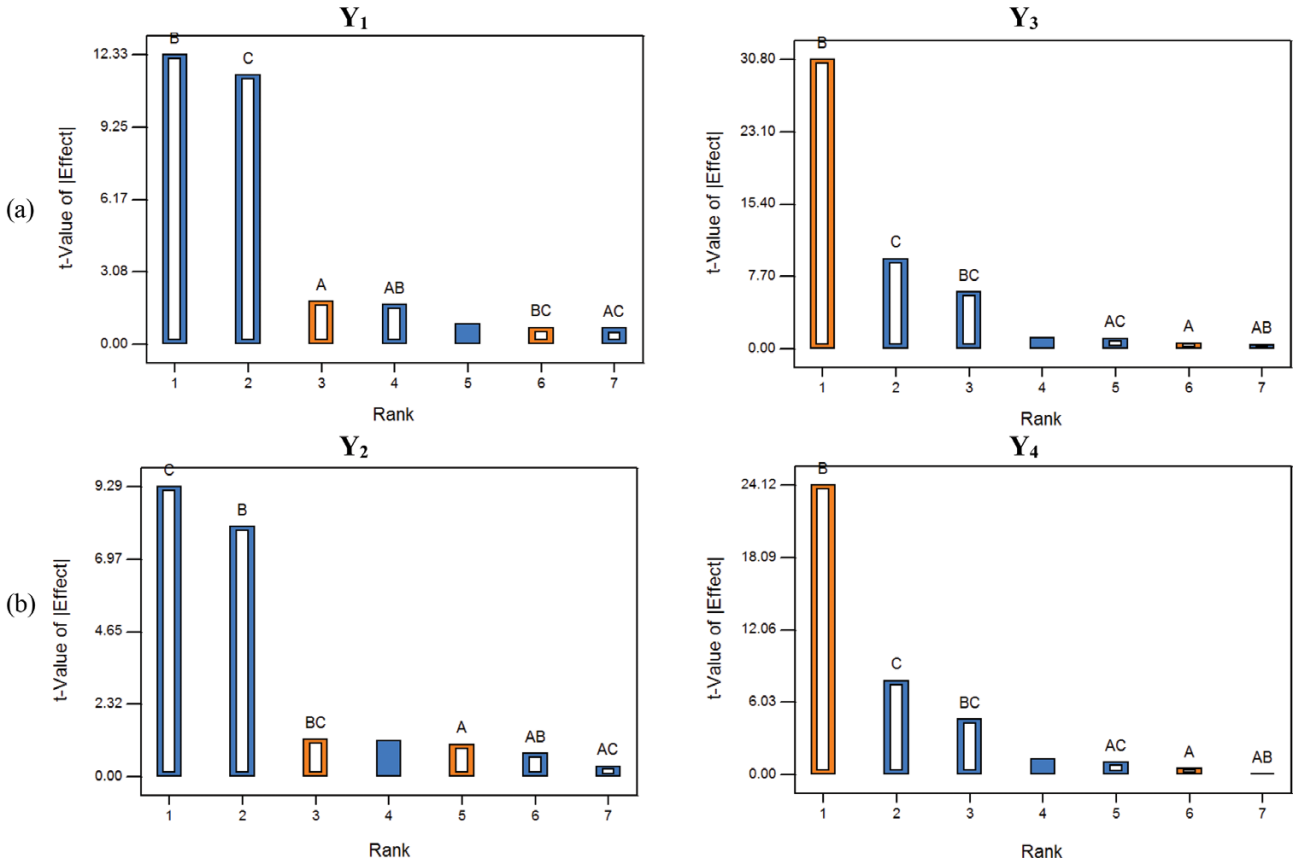


Fig. S4. Pareto diagram for (a) UMLDH and (b) CMLDH MO removal efficiency models, respectively.

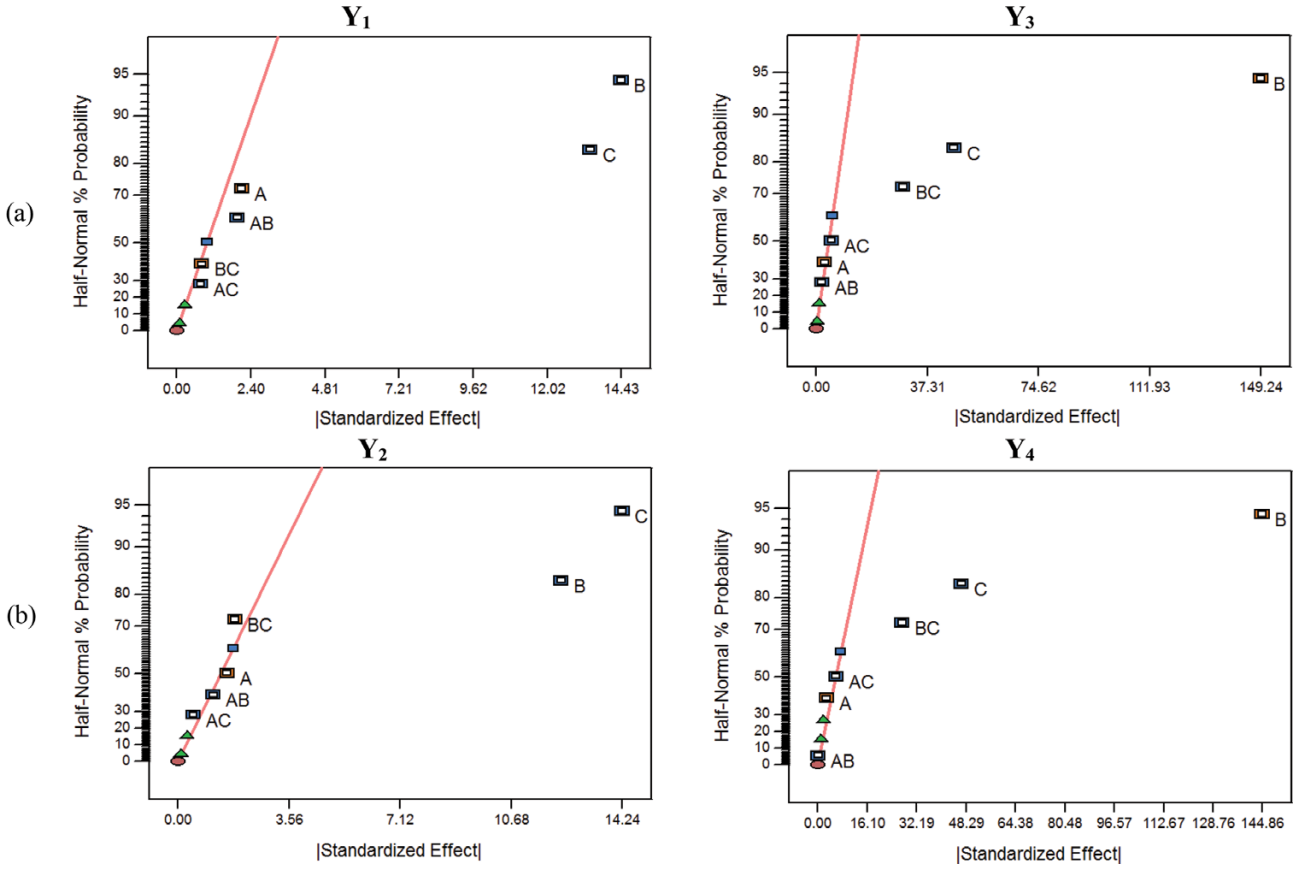


Fig. S5. Probability normal plots for (a) UMLDH and (b) CMLDH MO adsorption capacity models, respectively.

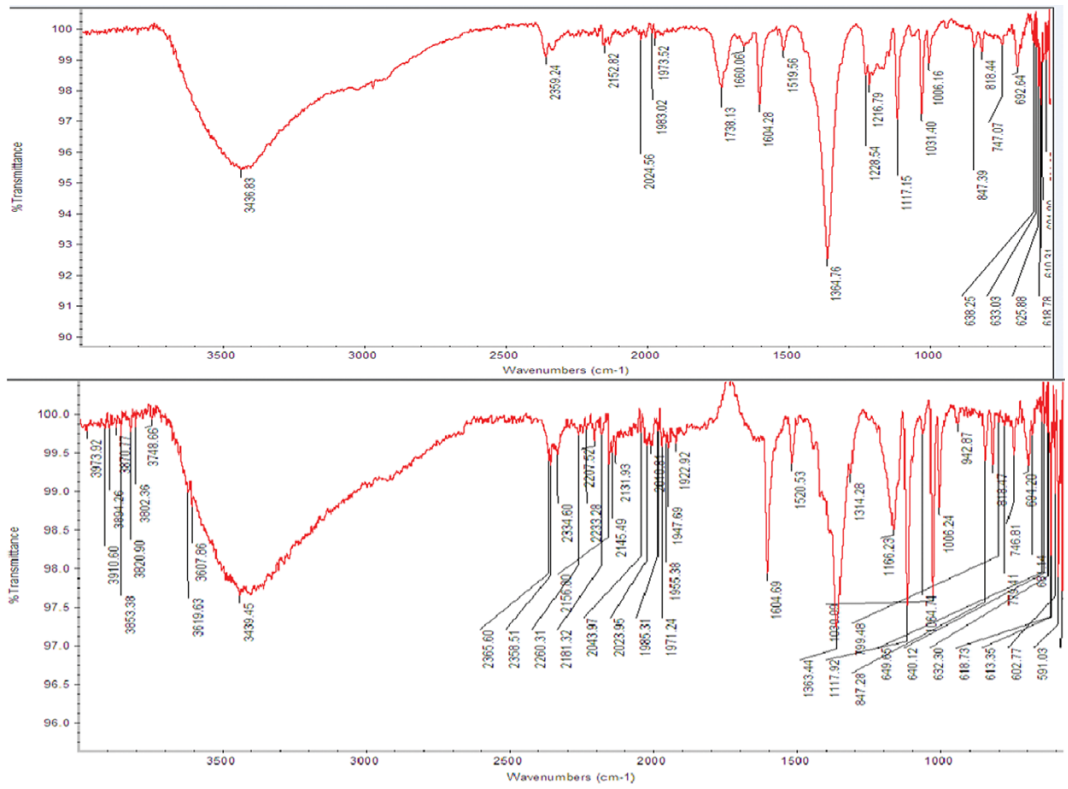


Fig. S6. FTIR patterns for the spent UMLDH (above) and CM-LDH (below) nanocomposites.

Table S1. BET surface area, pore volume and size distribution for UMLDH and CMLDH

Quantachrome NovaWin - Data Acquisition and Reduction
for NOVA instruments
©1994-2013, Quantachrome Instruments
version 11.03

Analysis Operator:	quantachrome	Date:2018/10/04	Report Operator:	quantachrome	Date:2019/06/18
Sample ID:	1	Filename:	uncalcined_magnetic_LDH.qps		
Sample Desc:		Comment:			
Sample weight:	0.0549 g	Sample Volume:	1 cc		
Outgas Time:	5.0 hrs	OutgasTemp:	150.0 C		
Analysis gas:	Nitrogen	Bath Temp:	273.0 K		
Press. Tolerance:	0.100/0.100 (ads/des)	Equil time:	60/60 sec (ads/des)	Equil timeout:	240/240 sec (ads/
Analysis Time:	179.8 min	End of run:	2018/10/04 5:10:39	Instrument:	Nova Station A
Cell ID:	0				

Data Reduction Parameters

t-Method	Calc. method: de Boer				
BJH/DH method	Moving pt. avg.: off	Ignoring P-tags below 0.35 P/Po			
Adsorbate	Nitrogen	Temperature	77.350K		
	Molec. Wt.: 28.013	Cross Section: 16.200 Å²		Liquid Density: 0.808 g/cc	

Radius Å	Pore Volume cc/g	Pore Surf Area m²/g	dV(r) cc/Å/g	dS(r) m²/Å/g	dV(logr) cc/g	dS(logr) cc/g
16.0849	7.0336e-03	8.7456e+00	2.8530e-03	3.5474e+00	1.0546e-01	1.3113e+02
18.7063	1.3855e-02	1.6038e+01	2.4558e-03	2.6257e+00	1.0558e-01	1.1289e+02
21.9105	2.2992e-02	2.4379e+01	2.5164e-03	2.2970e+00	1.2667e-01	1.1562e+02
26.1025	3.6300e-02	3.4576e+01	2.8000e-03	2.1454e+00	1.6782e-01	1.2859e+02
31.7401	5.8787e-02	4.8745e+01	3.4477e-03	2.1724e+00	2.5108e-01	1.5821e+02
40.4202	1.0160e-01	6.9931e+01	3.9507e-03	1.9548e+00	3.6548e-01	1.8084e+02
54.7741	1.7761e-01	9.7683e+01	4.2532e-03	1.5530e+00	5.3163e-01	1.9412e+02
81.8414	3.1958e-01	1.3238e+02	3.9150e-03	9.5672e-01	7.2553e-01	1.7730e+02

BJH adsorption summary

Surface Area =	132.378 m²/g
Pore Volume =	0.320 cc/g
Pore Radius Dv(r) =	54.774 Å

Quantachrome NovaWin - Data Acquisition and Reduction
for NOVA instruments
©1994-2013, Quantachrome Instruments
version 11.03

Analysis Operator:	quantachrome	Date:2018/10/04	Report Operator:	quantachrome	Date:2019/06/18
Sample ID:	1	Filename:	calcined_magnetic_LDH.qps		
Sample Desc:		Comment:			
Sample weight:	0.1053 g	Sample Volume:	1 cc		
Outgas Time:	5.0 hrs	OutgasTemp:	150.0 C		
Analysis gas:	Nitrogen	Bath Temp:	273.0 K		
Press. Tolerance:	0.100/0.100 (ads/des)	Equil time:	60/60 sec (ads/des)	Equil timeout:	240/240 sec (ads/des)
Analysis Time:	168.1 min	End of run:	2018/10/04 8:31:45	Instrument:	Nova Station A
Cell ID:	0				

Data Reduction Parameters

t-Method	Calc. method: de Boer				
BJH/DH method	Moving pt. avg.: off	Ignoring P-tags below 0.35 P/Po			
Adsorbate	Nitrogen	Temperature	77.350K		
	Molec. Wt.: 28.013	Cross Section: 16.200 Å²		Liquid Density: 0.808 g/cc	

Radius Å	Pore Volume cc/g	Pore Surf Area m²/g	dV(r) cc/Å/g	dS(r) m²/Å/g	dV(logr) cc/g	dS(logr) cc/g
16.1749	3.6697e-03	4.5375e+00	1.5498e-03	1.9164e+00	5.7619e-02	7.1245e+01
18.7243	7.9318e-03	9.0900e+00	1.5606e-03	1.6669e+00	6.7166e-02	7.1742e+01
21.9985	1.4200e-02	1.4789e+01	1.6420e-03	1.4928e+00	8.2965e-02	7.5428e+01
26.1332	2.2192e-02	2.0905e+01	1.7952e-03	1.3739e+00	1.0776e-01	8.2470e+01
31.6790	3.5784e-02	2.9486e+01	2.0471e-03	1.2924e+00	1.4878e-01	9.3928e+01
40.2425	6.1015e-02	4.2026e+01	2.4059e-03	1.1957e+00	2.2166e-01	1.1016e+02
54.5341	1.1119e-01	6.0428e+01	2.7729e-03	1.0169e+00	3.4497e-01	1.2652e+02
81.9193	2.2592e-01	8.8438e+01	3.1282e-03	7.6373e-01	5.8007e-01	1.4162e+02

BJH adsorption summary

Surface Area =	88.438 m²/g
Pore Volume =	0.226 cc/g
Pore Radius Dv(r) =	81.919 Å

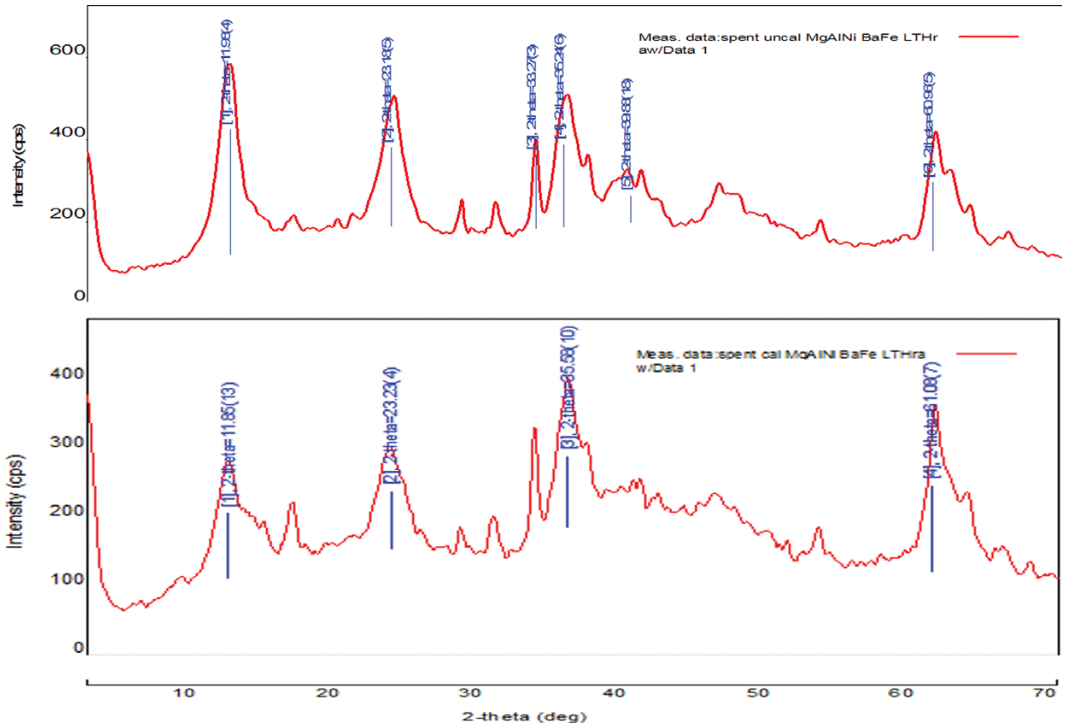


Fig. S7. XRD patterns for the spent UMLDH (above) and CMLDH (below) nanocomposites.

Table S2. UMLDH and CMLDH optimization goals, results and desirability for the different target scenarios

Variable	Scenario and its target goals				Optimization results							
					UMLDH				CMLDH			
	1	2	3	4	1	2	3	4	1	2	3	4
A	Minimize	Minimize	Minimize	In range	25	25	25	45	25	25	25	45
B	20	60	100	In range	20	60	100	100	20	60	100	100
C	In range	In range	In range	In range	4	4	4	4	4	4	4	4
Y_1	Maximize	Maximize	Maximize	Maximize	63.3	51.006	51.307	51.5988	-	-	-	-
Y_2	Maximize	Maximize	Maximize	Maximize					60.435	49.55	49.93	50.701
Y_3	Maximize	Maximize	Maximize	Maximize	106.93	184.47	276.37	279.571				
Y_4	Maximize	Maximize	Maximize	Maximize					103.91	177.95	267.42	273.02
Desirability	-	-	-	-	0.620	0.713	0.850	0.793	0.629	0.725	0.863	0.824

Table S3. UMLDH and CMLDH optimization goals, results and desirability for the different target scenarios

Variable	Scenario and its target goals				Optimization results							
					UMLDH				CMLDH			
	1	2	3	4	1	2	3	4	1	2	3	4
A	In range	In range	In range	In range	45	45	45	45	45	45	45	45
B	20	60	100	In range	20	60	100	100	20	60	100	100
C	In range	In range	In range	In range	4	4	4	4	4	4	4	4
Y_1	Maximize	Maximize	Maximize	Maximize	67.569	53.282	51.598	51.598	-	-	-	-
Y_2	Maximize	Maximize	Maximize	Maximize	-	-	-	-	63.681	51.476	50.701	50.701
Y_3	Maximize	Maximize	Maximize	Maximize	113.00	189.19	279.57	279.571	-	-	-	-
Y_4	Maximize	Maximize	Maximize	Maximize	-	-	-	-	108.83	183.37	273.02	273.02
Desirability	-	-	-	-	0.513	0.641	0.793	0.793	0.518	0.654	0.824	0.824